

Article

Effect of Grain Size on the Properties of Aluminum Matrix Composites with Graphene

Irina Brodova ¹, Liudmila Yolshina ², Sergey Razorenov ³, Dmitriy Rasposienko ¹, Anastasia Petrova ^{1,*}, Irina Shirinkina ¹, Evgeny Shorokhov ⁴, Roman Muradymov ², Gennady Garkushin ³ and Andrey Savinykh ³

¹ M.N. Mikheev Institute of Metal Physics, Ural Branch of Russian Academy of Sciences, 18 S. Kovalevskoy St., 620108 Ekaterinburg, Russia; ibrodova@mail.ru (I.B.); dmitrijrjasp@gmail.com (D.R.); shirinkina@imp.uran.ru (I.S.)

² Institute of High-Temperature Electrochemistry, Ural Branch of Russian Academy of Sciences, 20 Akademicheskaya St., 620137 Ekaterinburg, Russia; yolshina@ihte.uran.ru (L.Y.); muradymov@ihte.uran.ru (R.M.)

³ Institute of Problems of Chemical Physics, Russian Academy of Sciences, 1 Academician, Semenov Ave., 142432 Chernogolovka, Russia; razsv@fcp.ac.ru (S.R.); garkushin@fcp.ac.ru (G.G.); savas@fcp.ac.ru (A.S.)

⁴ Russian Federal Nuclear Center—Zababakhin All—Russia Research Institute of Technical Physics, P.O. Box 245, 456770 Snezhinsk, Russia; e.v.shorokhov@vniitf.ru

* Correspondence: petrovanastya@yahoo.com

Abstract: The structure and mechanical properties of composites consisting of a metal matrix based on aluminum and its alloys of different compositions (AA-3003 and AA-5154) and graphene synthesized in situ under a layer of molten salts were investigated depending on the chemical composition and grain size of the matrix. Aluminum matrix composites of three compositions were studied in as-cast coarse-grained, deformed fine-grained (grain size < 1 μm), and deformed sub microcrystalline (grain size < 1 μm) states in order to compare the structural characteristics of composites with different grain sizes. The composites were subjected to deformation with a split Hopkinson (Kolsky) bar and to dynamic-channel angular pressing. The hardness and dynamic mechanical properties of the composites were measured at strain rates $\dot{\epsilon}$ from $1.8 - 4.7 \times 10^3$ to $1.6 - 2.4 \times 10^5 \text{ s}^{-1}$. It was found that grain refinement induced a sharp increase in the hardness of composites with various compositions (by a factor of 1.6–2.6). A correlation of the elastic-plastic properties of the aluminum matrix composites with the grain sizes and chemical compositions of the matrices was established. A transition from coarse-grained to sub microcrystalline structure was shown to improve the elastic-plastic properties on average by a factor of 1.5. It was proved that the reinforcing effect of graphene increased with the decreasing grain size of the matrix. Mechanisms of reinforcement of the aluminum matrix composites using graphene were proposed.

Keywords: composite; graphene; structure; dynamic properties; transmission electron microscopy; hardness



Citation: Brodova, I.; Yolshina, L.; Razorenov, S.; Rasposienko, D.; Petrova, A.; Shirinkina, I.; Shorokhov, E.; Muradymov, R.; Garkushin, G.; Savinykh, A. Effect of Grain Size on the Properties of Aluminum Matrix Composites with Graphene. *Metals* **2022**, *12*, 1054. <https://doi.org/10.3390/met12061054>

Academic Editors: Massimo Pellizzari and Frank Czerwinski

Received: 25 April 2022

Accepted: 17 June 2022

Published: 20 June 2022

Publisher's Note: MDPI stays neutral with regard to jurisdictional claims in published maps and institutional affiliations.



Copyright: © 2022 by the authors. Licensee MDPI, Basel, Switzerland. This article is an open access article distributed under the terms and conditions of the Creative Commons Attribution (CC BY) license (<https://creativecommons.org/licenses/by/4.0/>).

1. Introduction

The interrelation of structure and properties has been proved in numerous research works in the field of materials science. In recent decades, techniques based on severe plastic deformation (SPD) have gained wide application and have made it possible to obtain metals and alloys with ultrafine grain sizes and to enhance physical and mechanical properties [1–4]. Severe straining with accumulated strain ϵ more than 1 is the basis of SPD methods. The main structural effects of SPD are ultrafine grain formation with sizes smaller than 1 μm, the dissolution of phases, supersaturated solid solution formation, precipitation, amorphization, the formation of deformation nanotwins and clusters, segregation, specific grain boundaries, and other crystal lattice defects. SPD methods include equal-channel angular pressing, high-pressure torsion, accumulative roll bonding, twist extrusion, radial

shear rolling, multi-axial forging, cyclic closed-die forging, cyclic extrusion compression, ball milling, repetitive side extrusion, continuous repetitive corrugating and straightening, and some of their modifications. Due to their numerous benefits, SPD methods have started to be widely used in the manufacture of construction materials, including metal matrix composites. In order to obtain materials with a desirable combination of plasticity and mechanical strength, one should carefully select the alloys used as the matrix, as well as the materials for its reinforcement. Aluminum alloys of various chemical compositions are widely used as the matrices of metal matrix composites since they offer a wide range of structural and functional properties [5–9]. For instance, aluminum composites reinforced with ceramic materials, oxides [5,6], and carbides [7] offer high strength, low density, high thermal conductivity, and very good corrosion resistance and tribological properties [8].

Researchers designing new, promising composite materials are currently concentrating their efforts on the production of composites reinforced with carbon-containing compounds—nanotubes, fullerenes, or graphene [10–14]. The latter is especially attractive as a reinforcing agent due to its unique properties, such as high mechanical hardness, high mobility of charge carriers, chemical stability, record high strength, and thermal conductivity [15]. According to the data reported in [16–20], there exist various techniques of introducing carbon nanomaterials into a metal matrix: infiltration of liquid metal into the fibers [16], ball milling [17], implantation of carbon ions into the Al target [18], selective laser melting [19], SPD [20], etc. Among new experimental methods of obtaining graphene-reinforced composites, one should mention the *in situ* synthesis of graphene nanoparticles from carbon-containing precursors directly in the metal matrix in molten salt media [21–25]. Among the key advantages of such a technique is the elimination of porosity, which is characteristic of composites produced *ex situ*, when previously obtained ultrafine nanoparticles are introduced into the metal matrix.

Designing new composite materials with the best possible functional properties requires information on the properties of the individual phases that constitute the fine structure of the composites and on the interactions of such phases with each other. In view of this, research into the relationship between the structural properties of the Al matrix (grain size, internal stresses, dislocation density, and phase composition) and the structure of the reinforcing additive, as well as its hardening capabilities, shows a lot of promise. In addition, one should determine the deformation mechanisms and the mechanisms of strengthening and investigate the way graphene affects the deformation behavior of aluminum matrix composites. For the most part, these issues have been addressed via computer simulation using methods of molecular dynamics and via theoretical simulation of the mechanical properties of metal matrix composites with graphene and carbon nanotubes [26–28]. Unfortunately, the available experimental data about the correlation between the structure of composites and their mechanical strengths are insufficient, and the available results are rather contradictory [29]. Initial studies of the structure formation of *in situ* composites based on aluminum and graphene have demonstrated both the positive effect of graphene as a reinforcing agent of aluminum matrix composites with disperse structure and the absence of reinforcement in the coarse-grained state [30,31].

In recent years, composites with heterogeneous laminated gradient structures have been created. It was established that they have an improved set of mechanical properties—high hardness, strength, and plasticity—at the same time. Such properties are associated with certain characteristics of the structure and appearance of additional hardening mechanisms. An example of such a composite is the heterogeneous TiBw/Ti-Ti(Al) composite with a layered arrangement of TiB whiskers synthesized through the diffusion annealing of stacked TiBw/Ti and Al foils [32]. The authors proved the important role of the influence of interfaces between the layers, as well as local deformation leading to microcracking, which changed the propagation of cracks in the composite. Another example is the creation of bimodal and trimodal metal matrix composites with carbon nanotubes (Al-Cu-Mg/CNT) [33]. The presence of layers with different grain sizes (coarse, fine, and ultrafine) in a trimodal Al-Cu-Mg/CNT composite prevented deformation localization and increased its plasticity.

The aim of the present work, formulated with the view of confirming these data and developing research in this field, is the investigation of specific features of the structure formation and static and dynamic mechanical properties of aluminum matrix composites with graphene synthesized in situ depending on the chemical compositions and grain sizes of the matrices.

2. Materials and Methods

Three different aluminum matrix composites alloyed with micro additions of graphene (0.10–0.12 wt.%) were the objects of the present study. The basic components of the composites were technical Al, an AA5154 aluminum alloy (Al-2.9% Mg), and an AA3003 aluminum alloy (Al-1.22%Mn) for AlGr, AlMgGr, and AlMnGr, respectively. The composites were synthesized through the interactions of molten Al alloys and different carbon-containing precursors under a layer of molten halide salts [21]. A schematic illustration of the synthesis of graphene nanofilms is given in [22]. Carbon-containing additives in the form of ascorbic acid, C-glucose, and boron carbide were used in the synthesis of the AlMgGr, AlGr, and AlMnGr composites, respectively. The synthesis temperature was 700–750 °C, and the holding times of liquid aluminum alloys of different compositions in the molten salt varied between 1 and 5 h. After the high-temperature treatment of the molten Al alloys in molten salt containing from 0.1 to 2 wt.% carbon-containing additives, the melt was poured into a corundum crucible and cooled at a rate of <1 deg/min. The synthesis of graphene nanosheets was a one-step process that took place directly in the molten alloy. First, carbon clusters started to appear as a part of the self-assembly process, followed by the formation of continuous films (nanosheets) uniformly distributed over the volume as the melt solidified. The chemical compositions of the materials obtained were studied using spectroscopic analysis with an ICPE-9000 SHIMADZU spectrometer (SHIMADZU CORPORATION, Kyoto, Japan) (± 0.005 wt.% uncertainty). Carbon inclusions in the composites were analyzed using energy-dispersive spectroscopy with a Quanta-200 scanning electron microscope (FEI Company, Hillsboro, OR, USA) and through Raman spectroscopy with a Renishaw U1000 instrument (Renishaw plc, Wotton-under-Edge, UK). The spectra were processed and analyzed with the help of built-in, Wire-30 software (Renishaw plc, Wotton-under-Edge, UK) using Fityk 0.9.8 data analysis.

For all the AlGr, AlMnGr, and AlMgGr composites, the Raman spectra of graphene were obtained. Figure 1 shows the Raman spectrum of graphene in the AlMnGr composite. The spectrum contained the characteristic peaks of sp^2 -hybridized carbon: D at 1345 cm^{-1} , G at 1580 cm^{-1} , and 2D at 2706 cm^{-1} . According to [34,35], the ratio of the I_{2D}/I_G and I_D/I_G peaks in the corresponding spectra indicated that the synthesis of the aluminum matrix composites yielded nanosheets of multilayer graphene varying in thickness and deficiency. Carbon inclusions in the AlGr composite synthesized from a glucose precursor could be described as defectless, three-layer graphene [30], while in the case of the AlMgGr composite with the ascorbic acid precursor, such inclusions presented double-layer graphene with defects in the structure. The synthesis of the AlMnGr composite with the boron carbide precursor yielded a double-layer, defectless graphene. Thus, by choosing different precursors, one could vary the structure of the graphene and the number of its layers in the composites. The influence of the multilayer graphene morphology on the structural features and properties of the aluminum matrix composites was not considered in this work.

Cylindrical samples with a coarse-grained (CG) structure weighing 100 g and having diameters of 45 mm and heights of 35 mm were obtained through casting in an alumina crucible. Aluminum matrix composites with fine-grained (FG) and sub microcrystalline (SMC) structures were produced using two methods of severe plastic deformation—dynamic compression in a split Hopkinson bar and dynamic-channel angular pressing. Samples for dynamic compression were cut from the casts of the aluminum matrix composites based on AD0 aluminum, Al-Mg, and Al-Mn alloys reinforced with 0.10–0.12% Gr. Samples for dynamic-channel angular pressing (DCAP) in the form of rods 14 mm in diameter and

100 mm in height were cast in a steel mold. Figure 2 contains a schematic of DCAP with a plunger [36,37]. The samples were accelerated to rates of $V = 215\text{--}300$ m/s with the help of a special gun and were directed into a die containing two channels of different diameters intersecting at an angle of 90° . Powder gases provided the energy for the acceleration of the samples. The samples were pressed in a setup with a plunger. The number of pressing cycles (N) was 2. In order to involve several shear planes, repeated pressing cycles according to the B_c route were performed in which the samples were rotated 90° clockwise around their axes between cycles, and the strain rate $\dot{\epsilon}$ was 10^4 s $^{-1}$.

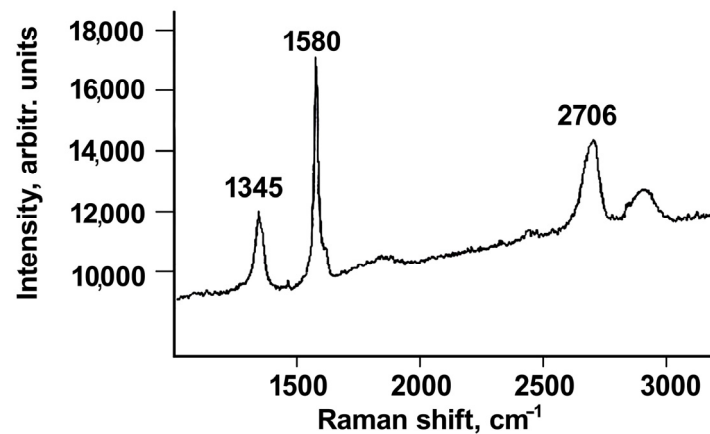


Figure 1. Raman spectrum of graphene in AlMnGr composite.

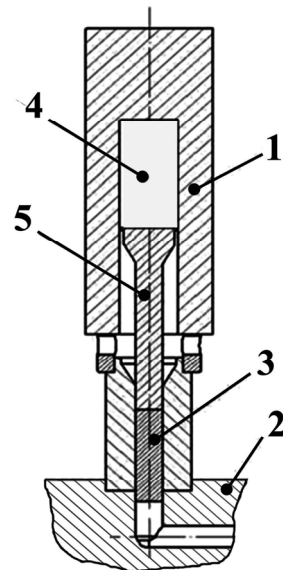


Figure 2. Schematic view of dynamic-channel angular pressing set up with plunger (1—barrel, 2—matrix, 3—sample, 4—powder charge, 5—plunger) [37].

The macrostructures of the samples were investigated using a NEOPHOT-32 optical microscope and a Quanta 200 scanning electron microscope fitted with an attachment for the automated indexing of electron backscatter diffraction (EBSD) maps. The data obtained were used to build histograms of grain–sub grain size distributions and misorientation angles of low-angle ($2\text{--}15^\circ$) and high-angle grain boundaries. The samples used in the structural analysis were prepared by mechanical grinding and subsequent polishing with a diamond suspension. The finishing polishing was carried out using a suspension of colloidal silicon dioxide. The fine structure of the samples was investigated with a Tecnai G 30 Twin transmission electron microscope (TEM) with a 300 kV accelerating voltage. Samples for the fine structure analysis were prepared by jet-polishing with a TenuPol-5 instrument in a solution of 20% nitric acid and 80% methanol (-25°C , 15–20 V).

The microhardness (Hv) was measured using a PMT-3 tester (Russia) with a load of 0.2 N (uncertainty not exceeding 10%), and the Brinell hardness was determined at a load of 250 kg with a 5 mm diameter ball. The dynamic properties of the AlGr composites and aluminum were measured over two ranges of strain rate $\dot{\epsilon}$: under the dynamic compression of samples with diameters of 8 mm and heights of 4 mm in a split Hopkinson (Kolsky) bar ($\dot{\epsilon} = 1.8 - 4.7 \times 10^3 \text{ s}^{-1}$; the velocity of the striker was 6.57–19.23 m/s) [38] and under the planar shock-wave loading of disk samples 0.9 mm in diameter ($\dot{\epsilon} = 1.6 - 2.4 \times 10^5 \text{ s}^{-1}$; the velocity of the striker was 620 m/s) [39,40].

3. Results and Discussion

Three different aluminum matrix composites were studied in as-cast coarse-grained (CG), deformed fine-grained (FG, grain size < 1 mm), and sub microcrystalline (SMC, grain size < 1 μm) states in order to compare the structure formation of composites with different grain sizes.

3.1. Structure and Properties of the Composites with Macrocrystalline (Coarse-Grained) Structure

Quantitative and qualitative metallographic analyses indicated that the crystallization mechanism and kinetics of the solid phase were unaffected by small amounts of multilayer graphene (0.1%) added to the aluminum matrix. The micrographs of the AlMgGr (Figure 3a) and AlMnGr (Figure 3b) samples demonstrated that their macrostructures were typical of aluminum alloys. The alternating zones and the sizes of the dendritic grains corresponded to the cooling rate of melts cast in a metal mold. The calculation of grain size in the as-cast composites and the as-cast graphene-free samples of the corresponding Al alloys showed that graphene was not an inoculant and did not modify the structure of the composites. The grain size in the AlGr and AlMnGr composites was 1000 μm , while in the AlGrMg composite, it was 500 μm . Graphene nanoplatelets were uniformly distributed over the volume of the ingot, and their lengths could reach up to tens of micrometers.

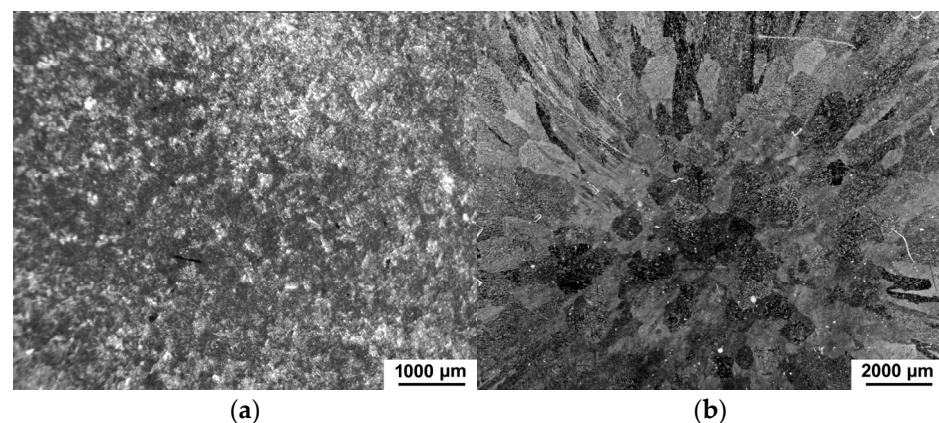


Figure 3. The macrostructures of the as-cast composites: (a) AlMgGr and (b) AlMnGr.

Table 1 contains the values of hardness for ingots of three compositions reinforced with graphene; the hardness of the composites in the as-cast state was seen to exceed the hardness of the corresponding unreinforced alloys by no more than 10%.

Table 1. Hardness of the ingots.

Matrix Composition	HB	
	without Graphene	with Graphene
Al	15	17
AlMg	62	64
AlMn	28	30

The dynamic properties of composites of different compositions were studied at the strain rate of $\dot{\epsilon} = 2.4 \times 10^5 \text{ s}^{-1}$. The dynamic elastic limit σ_{HEL} and yield strength Y were determined from the elastic precursor front amplitude measured from the free-surface wave profiles (see HEL point in Figure 11 as an example). The critical (breaking point) stresses on spallation (spall strength σ_{sp}) were determined using velocity recession from its maximum to the first minimum at the instant of spallation (see ΔU_{fs} in Figure 11 as an example). The given formulas of (1)–(3) were used for the calculation of dynamic characteristics [39–41].

$$\sigma_{HEL} = \rho_0 c_L U_{fs}^{HEL} / 2 \quad (1)$$

where ρ_0 is the initial density of the material, c_L is the longitudinal sound velocity in the material, and U_{fs}^{HEL} is the free-surface velocity behind the front of the elastic precursor.

$$\sigma_T = \frac{3}{2} \sigma_{HEL} \left(1 - c_B^2 / c_L^2 \right) \quad (2)$$

where c_B is the bulk velocity of sound.

$$\sigma_{sp} = 1/2 \rho_0 c_B (\Delta U_{fs} + \delta U) \quad (3)$$

where ΔU_{fs} is the decrement of the surface velocity upon decreasing the velocity from the maximum to the value in front of the spall pulse, and δU is the correction for the distortion of the wave profile because of the difference between the front velocity of the spall pulse and the velocity of the plastic part of the incident rarefaction wave in front of it [39–41].

The calculation results are presented in Figure 4. It was found that alloying the Al matrix with magnesium resulted in an increase in σ_{HEL} from 131 to 340 MPa and in Y from 57 to 170 MPa, i.e., by a factor of 2.6. Alloying with manganese improved the elastic-plastic properties by a factor of 2. The dynamic strength of there in forced composites was 1130–1560 MPa.

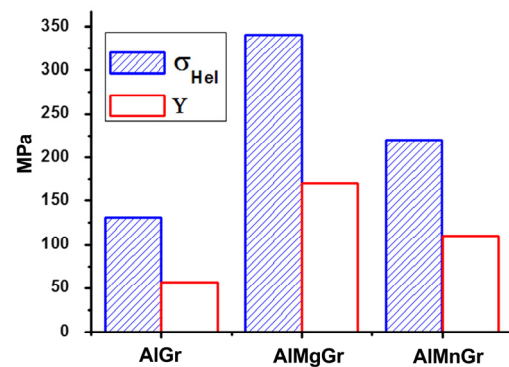


Figure 4. Dynamic properties of CG composites.

3.2. Structure and Properties of the Composites with Microcrystalline (Fine-Grained) Structure

Composites with fine-grained (FG) structures and grain sizes $< 1 \text{ mm}$ were produced by dynamic compression in a split Hopkinson bar. Let us consider the evolution of the structure upon dynamic deformation with a split Hopkinson bar (Figure 5) on the example of the AlMgGr composite. Because of the non-uniform nature of the high-speed deformation, different zones formed in the structure of the composite, which consisted of elongated grains of 200–500 μm in size with developed inner substructures and a small number of equiaxed fine grains of 5–10 μm in size (Figure 5a). Thin layers of a modified eutectic consisting of intermetallic compounds of Al(Fe, Mn, Si) and Mg_2Si were retained along the grain boundaries (Figure 5b). According to the EDS analysis, the content of the elements at point 1 was 73.9 at.%Al, 8.22 at.%Si, 5.92 at.% Mn, and 11.96 at.%Fe, which corresponded to the $(\text{FeMn})_3\text{Si}_2\text{Al}_{15}$ phase. The content at point 2 was 20.35 at.%Mg and 9.10 at.%Si, which corresponded to the Mg_2Si phase. According to the EBSD data, more than half of the

grains–subgrains in the area with deformed FG structure were less than 25 μm in size, the average grain–subgrain size being 50 μm ; the ratio between the high-angle and low-angle boundaries was 20:80, and the average misorientation angle was 10–15°.

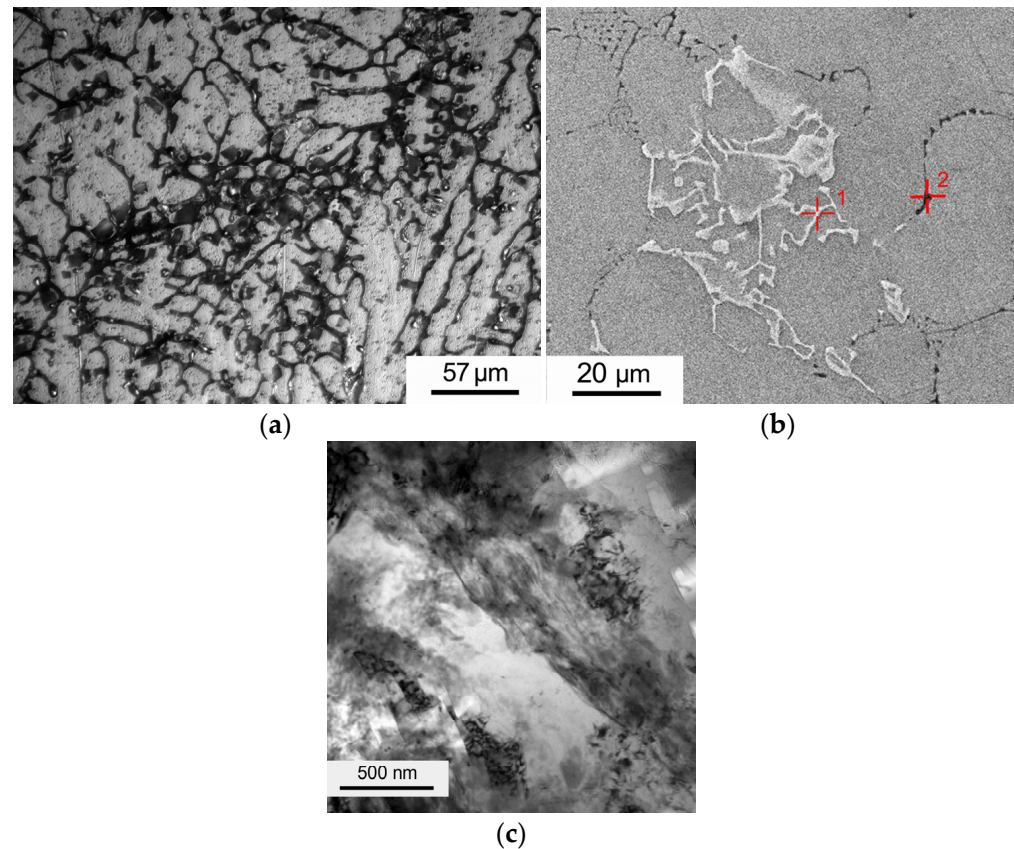


Figure 5. AlMgGr composite structure after dynamic compression: (a)—zones with various grain morphologies; (b)—eutectic; (c)—area of fragmented structure (TEM).

The image of such a structure is given in Figure 5c. The equiaxed grains without an inner substructure surrounded by HABs were likely formed via dynamic recrystallization upon compression. Thus, the deformed composite had a mixed FG structure consisting of large, fragmented grains and small, recrystallized grains whose volume fractions depended on the degree of deformation. For example, with a relative deformation not exceeding 40%, their volume fraction was no more than 10%. Such a structure is typical of many Al alloys that undergo high-rate deformation under quasi-static conditions [37,38]. The analysis of the structure of the deformed composites pointed to the fact that reinforcement with graphene did not affect the dislocation density or the deformation mechanism in the matrix.

The deformation of graphenenanoplatelets was highly inhomogeneous under dynamic compression. Most of them retained the shapes and sizes characteristic of the as-cast state, while others rolled up, broke, and overlapped. The arrangement of the nanoplatelets in the deformed structure of the composites depended on the composition of the matrix. They resided mainly along the grain boundaries or inside the Al matrix grains, but in the alloyed composites, they were also found on the fragments of the brittle intermetallic crystals. Thus, the TEM images of the AlGr composite showed irregularly faceted structural elements (Figure 6a) that, according to the dark-field images (Figure 6b) and the analysis of the direct images of the crystal structure (Figure 6c,d, [30]), could be identified as graphenenanoplatelets.

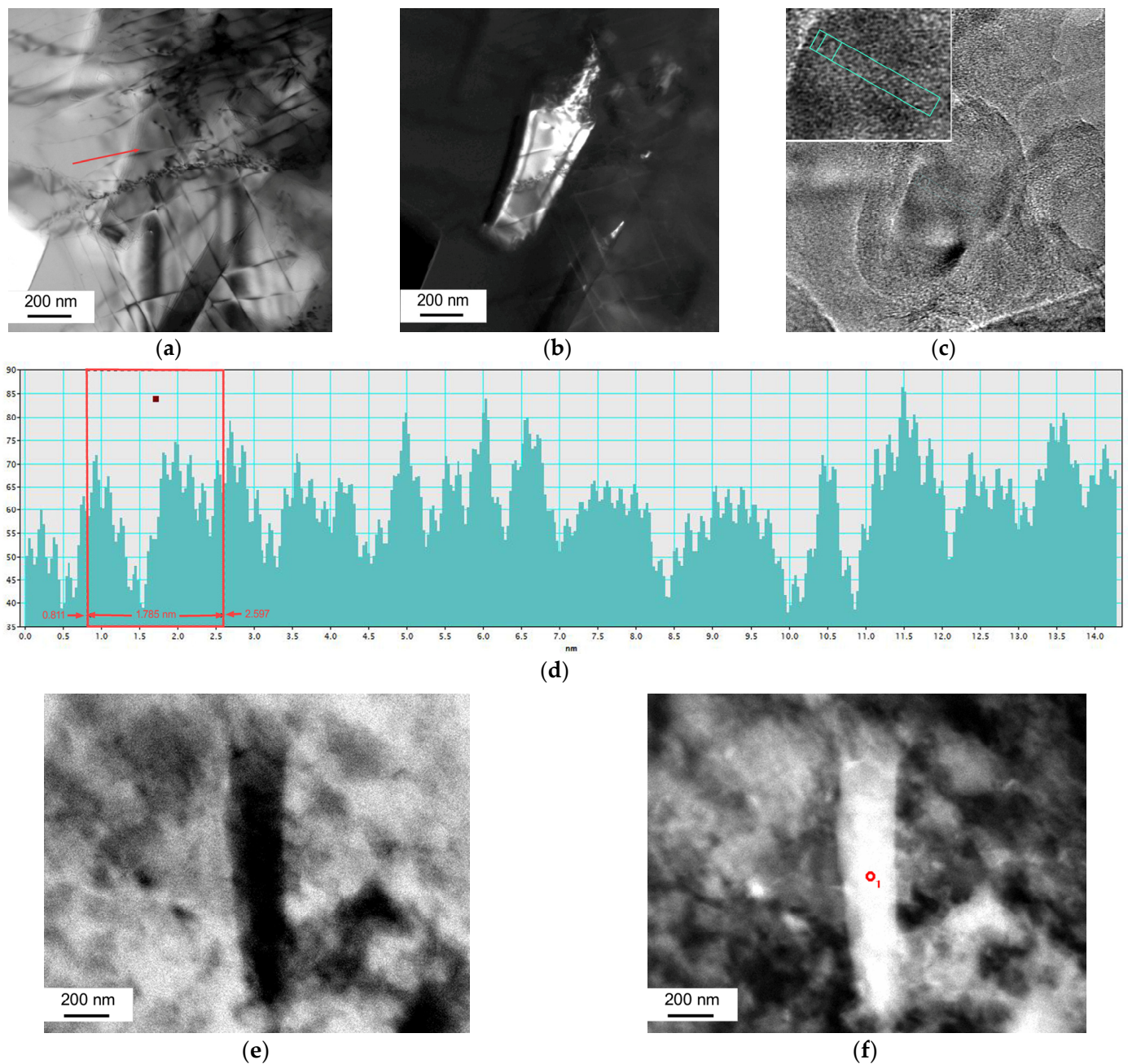


Figure 6. Fragments of graphene nanoplatelets in (a–d) AlGr composite and (e,f) AlMgGr composite after Hopkinson bar compression tests: (a) bright-field image and (b) dark-field image in reflections of $(100)_{Gr}$. (c,d) Direct imaging of graphene crystal structure: (c) inverse Fourier transform of the image, $d = 0.31785$ nm; (d) intensity histogram ($10d = 1.785$ nm). (e) Bright-field STEM image and (f) dark-field image.

Figure 6e shows a fragment of the AlMgGr structure. Platelet-shaped crystals of the Al(Fe,Si) aluminide are visible in the bright-field image. Due to the difference in the diffraction contrast, the dark-field STEM images demonstrated lighter films on these crystals (Figure 6f). Local chemical analysis (Figure 6f, point 1) revealed the presence of a large amount of carbon (about 40–50 at.%) alongside iron, aluminum, and silicon, which indicated that graphene may reside on the surface of brittle intermetallics. Refinement of the structure relative to the as-cast state induced by dynamic compression (down to 100–50 μ m) led to minor changes in the hardness and microhardness of the matrices. The

hardness of the AlGr composite increased by 25%, while the microhardness of the AlMgGr composite matrix increased by no more than 15–20%.

The mechanical properties of FG composites with different compositions were determined at quasi-static strain rates of $1.3 - 4.7 \times 10^3 \text{ s}^{-1}$, whereby the relative compression of the samples did not exceed 35–45%. The offset yield strength and offset tensile strength were determined based on the stress–strain diagrams of dynamic compression. The data for the dynamic properties of composites with different compositions were averaged over the experimental range of the strain rates and compared with each other and with the properties of corresponding unreinforced materials. No difference was found between the dynamic properties of the AlGr composite and unreinforced Al. The offset yield strength σ_T was 41 MPa, and the offset tensile strength σ_B was 104 MPa. In the case of the aluminum–magnesium alloy, the characteristics of the composites were enhanced by a factor of 2.8 and reached $\sigma_T = 114 \text{ MPa}$ and $\sigma_B = 298 \text{ MPa}$, but compared to the unreinforced AlMg alloy, their growth was 5–8%. These results indicated that it was the composition of the matrix that determined the considerable differences in the mechanical properties of the aluminum matrix composites.

3.3. Structure and Properties of the Composites with Submicrocrystalline Structure

Investigation into the evolution of the structural, physical, and mechanical properties of Al and its alloys revealed that the structure refinement mechanisms in the alloys subjected to DCAP depended on the nature of the alloys, which were characterized by the varying mobility of the dislocation ensemble [37]. To investigate the role of this factor in structure formation upon dynamic compression of the aluminum matrix composites, the authors chose alloys with different compositions of matrices, i.e., AlGr and AlMnGr. The non-heat-hardenable Al–Mn alloy with weak solid solution strengthening was characterized by a lower dislocation mobility than Al with a high stacking-fault energy of $\gamma = 200 \text{ mJ/m}^2$. The EBSD analysis (Figure 7a,b) showed that, after two cycles of high strain-rate deformation, the structure of the AlMnGr composite was formed by shear mesobands that were 300–700 μm wide. Alternation of bands consisting of fragmented grains–subgrains with a large number of low-angle boundaries (LABs) was observed. Inside the shear mesobands, one could see a less distinct alternation of bands formed by LABs with 5–15° misorientations.

Fine-equiaxed grains produced via dynamic recrystallization formed along the high-angle elongated boundaries. The average grain–subgrain size in such a mixed structure was 270 nm, whereby grains–subgrains less than 100 nm in size made up 40–50% (Figure 7c). The number of HABs did not exceed 15%, and the majority of the boundaries were LABs with misorientation angles $< 5^\circ$ (Figure 7d). The presence of such boundaries indicated a high dislocation density, which is characteristic of a deformed structure. The dislocation density calculated from the broadening of the diffraction peaks from the planes of the fcc lattice was $\rho = 3 - 4 \times 10^{10} \text{ cm}^{-2}$, which confirms the dislocation nature of the LABs.

Figure 8 shows the developed grain–subgrain structure of the AlMnGr composite after DCAP.

The TEM examination confirmed that the deformation treatment resulted in a composite with a banded anisotropic structure consisting of mesobands that were 10–12 μm long and 2–4 μm wide (Figure 8a). Along the edges of the deformation bands, one could observe the presence of the $\text{Al}_6(\text{Fe, Mn})$ phase in the form of continuous films up to 4 μm long and 0.07 μm thick, which formed in the course of the crystallization of the alloy (Figure 8b,c). These large inclusions were retained upon the subsequent deformation, and as a result, HABs became firmly positioned along the boundaries of the previously existing grains.

The mesobands consisted of elongated subgrains up to 0.7–1.0 μm long and 0.3–0.7 μm thick (Figure 8d). More disperse subgrains formed along the edges of the bands or around the intragranular precipitates of the $\text{Al}_6(\text{Fe, Mn})$ phase, which was partly broken and dissolved by the deformation, acquiring the shape of globules up to 0.5 μm in diameter. The dark-field images in the $(111)_{\text{Al}}$ reflections clearly demonstrated that part of the subgrains were broken into fragments of 150 to 700 nm separated by low-angle boundaries

(Figure 8d). The majority of the subgrains and fragments were characterized by high dislocation density (Figure 8e). Despite the similarities in the structure formation of different composites under dynamic compression, the EBSD analysis of the AlGr composite revealed a number of important differences. Mesobands with a recrystallized structure became the main structural constituent, there was a change in the ratio between HABs and LABs, the dislocation density decreased, and the average grain–subgrain size increased (Table 2).

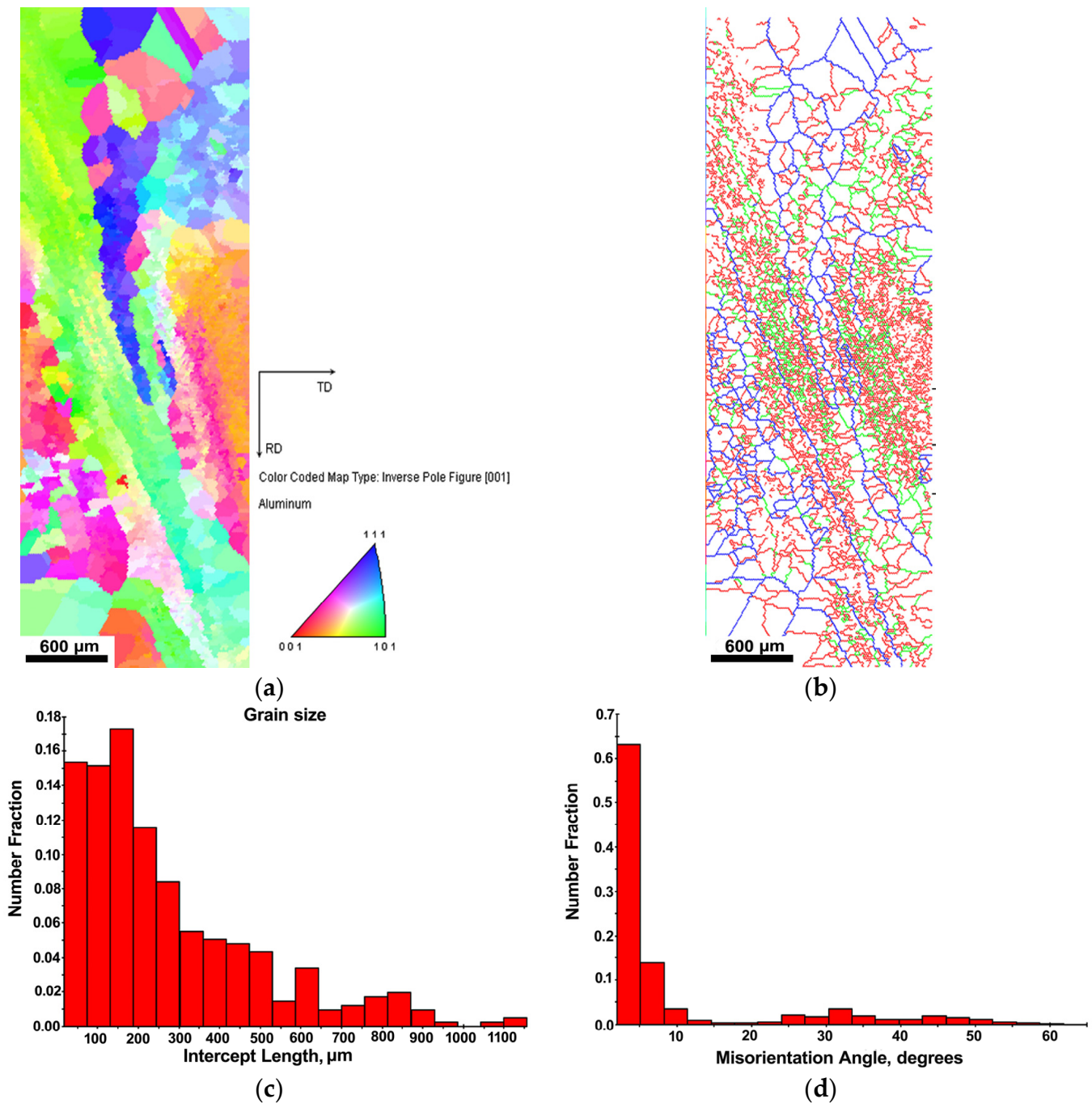


Figure 7. EBSD analysis of AlMnGr composite: orientation map (a); grain boundary map (HABs > 15° are in blue, LABs > 5° are in green, and LABs < 5° are in red) (b); histogram of grain–subgrain size distributions (c); misorientation angles (d).

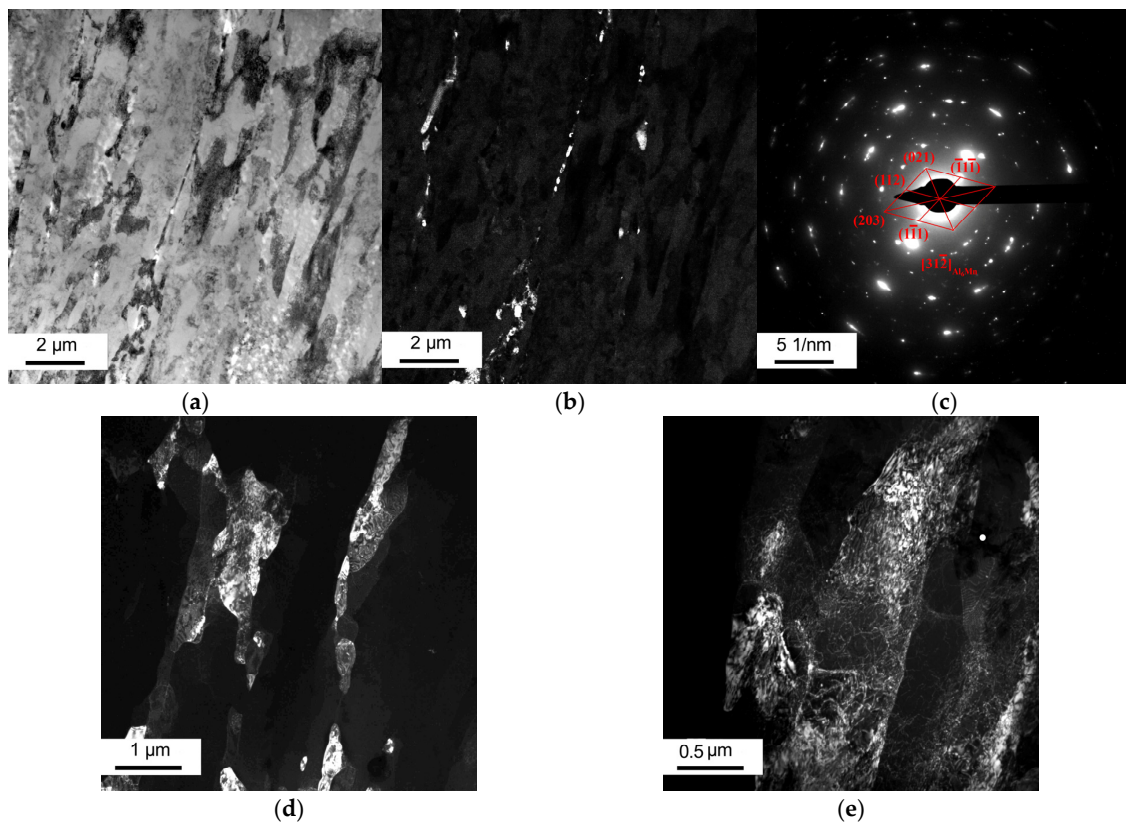


Figure 8. AlMnGr composite microstructure after DCAP: bright-field image (a) and dark-field images (b,d,e) (b) in $(311)_{Al_6Mn}$ reflection and (d,e) in $(111)_{Al}$ reflections; electron diffraction pattern with Al_6Mn reflections (c), $[312]$ zone axis.

Table 2. Characteristics of the fine-structured composites.

Composition	LABs (2–5°)	LABs (5–15°)	HABs (>15°)	Average Grain–Subgrain Size, μm	Hardness, MPa
AlGr	38	8	54	2.0	4.5
AlMgGr	70	14	15	0.3	5.0

Figure 9 shows the submicrocrystalline structure of the AlGr composite. The lighter contrast of the graphene films made it possible to determine their morphologies and locations. They were visualized as rectangles from 100 to 250 nm in size and were found both along the dislocation boundaries and inside the grains (Figure 9a,b).

Thus, a more disperse, fragmented SMC structure formed mainly through fragmentation was predominant in the composites with the Al–Mn matrix, while in the AlGr composites, dynamic recrystallization was the main mechanism of energy dissipation upon deformation.

The hardness of the composites also depended on their compositions and structural properties. A comparison of the hardness values for the CG and SMC composites demonstrated that structure refinement resulted in an increase in their hardness by factors of 1.6 (AlMnGr) and 2.6 (AlGr) (Figure 10).

In addition to measuring the strength characteristics of the studied composites under quasi-static loads, measurements of the properties of SMC composites (dynamic elastic limit σ_{HEL} and dynamic yield strength Y) under shock-wave loadings with $\geq 10^5 \text{ s}^{-1}$ were performed. The method of determining the strength characteristics under shock loading

was based on the analysis of the free-surface velocity profiles of the shock-compressed samples recorded upon loading using a VISAR laser interferometer [42].

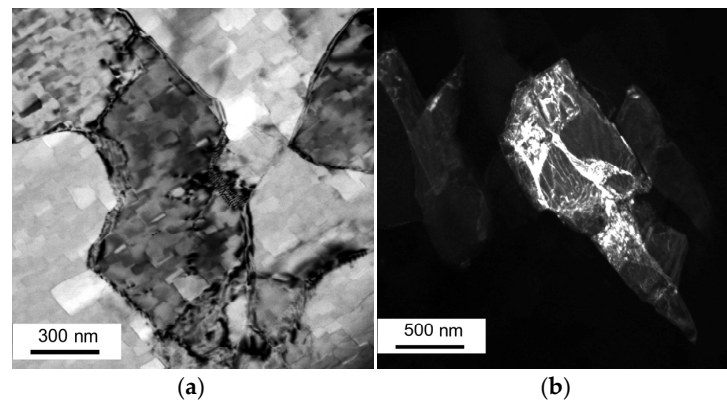


Figure 9. Dislocation structure of SMC AlGr composite after DCAP: bright-field image (a) and dark-field image in $(111)_{Al}$ reflection (b).

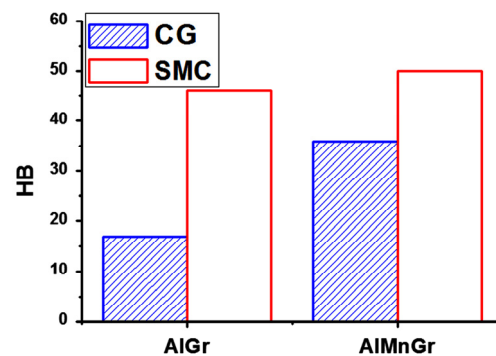


Figure 10. The hardness of aluminum matrix composites with different grain sizes.

Figure 11 contains free-surface velocity profiles of the SMC AlGr (Profile 1) and the SMC AlMnGr (Profile 3). In order to evaluate the deformation behavior of the SMC composites and specific features of their destruction, a comparison with their CG analogs was made (Profile 2). The release of an elastic precursor propagating with a longitudinal sound velocity c_l was recorded on all the free-surface velocity profiles.

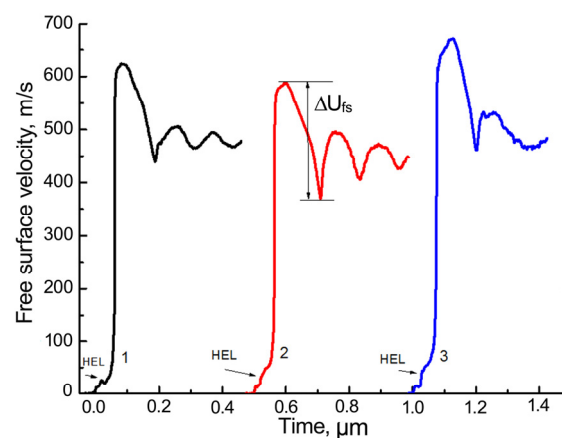


Figure 11. Free surface velocity profiles for the composites: 1—SMC AlGr; 2—CG AlMnGr; and 3—SMC AlMnGr.

The data for the calculation of the elastic-plastic properties σ_{HEL} and Y for the SMC composites are given in a histogram (Figure 12). The experimental results allowed us to ex-

amine the difference between the properties of aluminum matrix composites with different matrices (AlMnGr and AlGr) obtained under similar deformation conditions. The dynamic properties of the SMC AlMnGr were rather high: $Y = 170$ MPa and $\sigma_{HEL} = 340$ MPa. The characteristics of the Al-based SMC composite reinforced with graphene could be described as inferior: $Y = 103$ MPa and $\sigma_{HEL} = 236$ MPa (i.e., the properties of the SMC composite based on the Al-Mn alloy were 1.4 times higher).

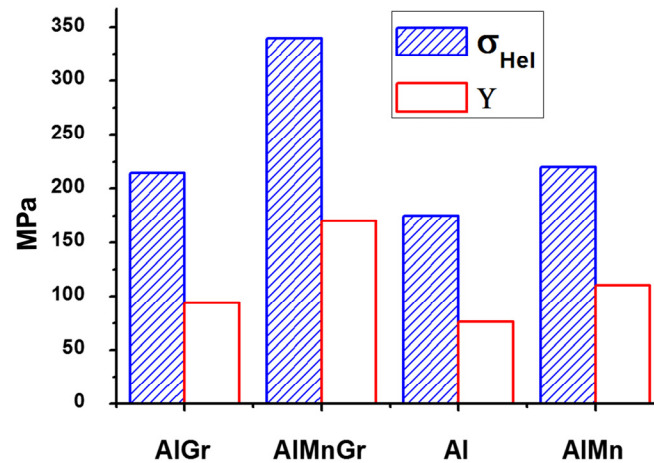


Figure 12. Dynamic properties of SMC composites and their SMC unreinforced analogs.

For a more correct assessment of the role that graphene played as a reinforcing agent of aluminum matrix composites, unreinforced samples were also subjected to DCAP. A comparison of the elastic-plastic properties of the SMC aluminum with the properties of the SMC AlGr composite showed that a 0.1% addition of graphene reinforced the material and increased σ_{HEL} and Y by 30%. The properties of the SMC AlMnGr composite surpassed those of the unreinforced SMC AlMn alloy by 50%.

In addition, values of critical fracture stresses (spall strength) for all the types of samples were determined from the measured free-surface velocity profiles. This value was proportional to the decrement in the surface velocity Δu_{fs} as it decreased from the maximum to the value before the front of the spall pulse (Figure 11). The enhancement of the elastic-plastic properties induced by alloying the Al matrix was accompanied by a 10–20% decrease in the shear strength. Its value for the graphene-doped samples was ~ 1.5 GPa and tended to slightly decrease with increasing graphene concentration since the graphene solid particles were stress concentrators upon dynamic tension under spall conditions. A decrease in the spall strength by 5–10% upon the transition from coarse-grained to SMC composite was related to the increasing area of the grain boundaries and the emergence of concentrators of additional tensile stresses on them due to hard graphene nanoplatelets.

If we compare the data relating to the AlGr and AlMnGr composites in Figures 3 and 12, we can observe that the structure refinement that accompanied the transition from the CG to the SMC state induced a sharp enhancement of elastic-plastic properties: by 63% in the AlGr composite and by 54% in the AlMnGr composite.

The results obtained indicate that the reinforcing ability of graphene increased with decreasing grain size in the matrix. The highest strengthening was observed in the case of SMC composites. In addition to strengthening through the Hall-Petch mechanism, additional strengthening channels appeared in SMC composites with graphene. From the analysis of the articles cited in the Introduction, it follows that the mechanical properties of composites depend on the synthesis conditions, the volume fraction of the graphene, the geometry and orientation of graphene nanoplatelets in the matrix, etc. Several hardening mechanisms could be distinguished: the load transfer to graphene nanoplatelets, the forma-

tion of Orowan loops, the formation of misfit dislocations due to different crystal lattices of graphene and the matrix, differences in thermal expansion coefficients, etc. [29,43].

The contribution of each mechanism to the overall hardening strongly depended on the location of graphene in the matrix and was different for layered composites and composites with homogeneous structures. For composites with a uniform arrangement of graphene in the matrix, two main strengthening mechanisms could be distinguished: the formation of Orowan loops when dislocations wrapped around microplatelets of graphene and the deceleration of dislocations near graphene plates. The first mechanism operated mainly in the presence of graphene plates inside the matrix grains, and the second was mainly associated with the presence of graphene on the grain boundaries. According to the TEM data, in aluminum matrix composites synthesized using our technology, graphene was located randomly; both on the boundaries and inside the grains of the matrix. Therefore, both mechanisms played an important role and were the reason for the increase in the mechanical properties of the composites compared to the unreinforced alloys.

Thus, the role of graphene was twofold: first, it was a source of misfit dislocations owing to the difference in the crystal structures of the Al matrix and graphene; secondly, dislocations piled up and created an obstacle at the Al matrix–Gr interphase, i.e., graphene nanoplatelets became a barrier to dislocation motion similar to the dispersed inclusions of intermetallic phases.

4. Conclusions

Graphene was not an inoculant and did not affect the grain size of the as-cast aluminum matrix composites. The hardness of the as-cast composites depended on the chemical compositions of the matrices and increased by 5–10% compared to the unreinforced Al alloys.

When an SMC structure was formed in the composites through high-rate deformation, graphene nanoplatelets broke up, bent, and primarily occupied positions along the grain–subgrain boundaries, providing an additional deformation mechanism of reinforcement due to contact with the dislocations.

The transition from the CG to the SMC state brought about a sharp increase in the hardness of the composites by a factor of 1.6 in the composites based on the Al–Mn alloy and by a factor of 2.6 in the AlGr composite.

The elastic–plastic properties of the aluminum matrix composites depended on the grain size and on the chemical compositions of the matrices and increased, on average, 1.5 times when the structure was refined to a submicron scale.

A comparison of the elastic–plastic properties of the SMC composites with the properties of the SMC unreinforced materials showed that a 0.1% addition of graphene strengthened the material and increased the σ_{HEL} and Y values by 30–50%, depending on the chemical composition of the matrix.

Author Contributions: Conceptualization, methodology, and writing, I.B.; methodology and material processing, L.Y., R.M. and E.S.; TEM investigation, D.R.; SEM investigation, I.S.; data processing, A.P.; measurement of properties and data processing, S.R., G.G. and A.S. All authors have read and agreed to the published version of the manuscript.

Funding: The results were obtained within the state assignments of the Ministry of Science and Higher Education of the Russian Federation (theme “Struktura” №122021000033-2 (IMP UB RAS), №122020100210-9 (IHTE UB RAS) and AAA-A19-119071190040-5 (IPCP RAS)).

Institutional Review Board Statement: Not applicable.

Informed Consent Statement: Not applicable.

Data Availability Statement: Not applicable.

Acknowledgments: The electron microscopic studies were performed at the Center of Collaborative Access’ Test Center of Nanotechnologies and Advanced Materials, Institute of Metal Physics, Ural Branch, Russian Academy of Sciences (RAS, Ekaterinburg, Russia). The shock-wave compression experiments were carried out using equipment at the Moscow Regional Explosive Research Center

for Collective Use, RAS (Chernogolovka, Russia). The Raman spectra for graphene were collected using equipment at the Shared Access Center for the Composition of Compounds, Institute of High-Temperature Electrochemistry, Ural Branch, RAS (Ekaterinburg, Russia).

Conflicts of Interest: The authors declare no conflict of interest.

References

1. Langdon, T.G. The principles of grain refinement in equal-channel angular pressing. *Mater. Sci. Eng. A* **2007**, *462*, 3–11. [[CrossRef](#)]
2. Zehetbauer, M.J.; Valiev, R.Z. *Nanomaterials by Severe Plastic Deformation*; Wiley: Weinheim, Germany, 2004.
3. Estrin, Y.; Vinogradov, A. Extreme grain refinement by severe plastic deformation: A wealth of challenging science. *Acta Mater.* **2013**, *61*, 782–817. [[CrossRef](#)]
4. Segal, V. Review: Modes and Processes of Severe Plastic Deformation (SPD). *Materials* **2018**, *11*, 1175. [[CrossRef](#)] [[PubMed](#)]
5. Mondolfo, L.F. *Aluminum Alloys: Structure and Properties*; Butterworth & Co.: Oxford, UK, 1976.
6. Wang, H.; Geng, H.; Liu, C. The influence of SiO₂ on the aluminum borate whisker reinforced aluminum phosphate wave-transparent materials. *Procedia Eng.* **2012**, *27*, 1222–1227. [[CrossRef](#)]
7. Khrustalev, A.P.; Kozulin, A.A.; Zhukov, I.A.; Khmeleva, M.G.; Vorozhtsov, A.B.; Eskin, D.G.; Chankitmongk, S.; Platov, V.V.; Vasilev, S.V. Influence of Titanium Diboride Particle Size on Structure and Mechanical Properties of an Al-Mg Alloy. *Metals* **2019**, *9*, 1030. [[CrossRef](#)]
8. Das, D.K.; Mishra, P.C.; Singh, S.; Thakur, R.K. Properties of ceramic-reinforced aluminium matrix composites—A review. *Int. J. Mech. Mater. Eng.* **2014**, *9*, 12. [[CrossRef](#)]
9. Zhukov, I.A.; Nikitin, P.Y.; Grigoriev, M.V.; Vorozhtsov, A.B. Phase composition and hardness of AlMgB14-based polycrystalline materials. *Russ. Phys. J.* **2019**, *62*, 882–885. [[CrossRef](#)]
10. Tjong, S.C. Recent progress in the development and properties of novel metal matrix nanocomposites reinforced with carbon nanotubes and graphenenanosheets. *Mater. Sci. Eng. R* **2013**, *74*, 281–350. [[CrossRef](#)]
11. Tabandeh-Khorshid, M.; Ajay, K.; Omrani, E.; Kim, C.; Rohatgi, P. Synthesis, characterization, and properties of graphene reinforced metal-matrix nanocomposites. *Composites B* **2020**, *183*, 107664. [[CrossRef](#)]
12. Khanna, V.; Kumar, V.; Bansal, S.A. Mechanical properties of aluminium-graphene/carbon nanotubes (CNTs) metal matrix composites: Advancement, opportunities and perspective. *Mater. Res. Bull.* **2021**, *138*, 111224. [[CrossRef](#)]
13. Bakshi, S.R.; Lahiri, D.; Agarwal, A. Carbon nanotube reinforced metal matrix composites—A review. *Int. Mater. Rev.* **2010**, *55*, 41–64. [[CrossRef](#)]
14. Hu, Z.; Tong, G.; Lin, D.; Chen, C.; Guo, H.; Xu, J.; Zhou, L. Graphene-reinforced metal matrix nanocomposites—A review. *Mater. Sci. Technol.* **2016**, *32*, 930–953. [[CrossRef](#)]
15. Papageorgiou, D.G.; Kinloch, I.A.; Young, R.J. Mechanical properties of graphene and graphene-based nanocomposites. *Prog. Mater. Sci.* **2017**, *90*, 75–127. [[CrossRef](#)]
16. Naplocha, K.; Granat, K. Dry sliding wear of Al/Saffil/C hybrid metal matrix composites. *Wear* **2008**, *265*, 1734–1740. [[CrossRef](#)]
17. Pérez-Bustamante, R.; Pérez-Bustamante, F.; Estrada-Guel, I.; Santillán-Rodríguez, C.R.; Matutes-Aquino, J.A.; Herrera-Ramírez, J.M. Characterization of Al₂₀₂₄-CNTs composites produced by mechanical alloying. *Powder Technol.* **2011**, *212*, 390–396. [[CrossRef](#)]
18. Uglov, V.V.; Cherenda, N.N.; Danilyuk, A.L.; Rauschenbach, B. Structural and phase composition changes in aluminium induced by carbon implantation. *Surf. Coat. Technol.* **2000**, *128–129*, 358–363. [[CrossRef](#)]
19. Hu, Z.; Chen, F.; Xu, J.; Nian, Q.; Lin, D.; Chen, C.; Zhu, X.; Chen, Y.; Zhang, M. 3D printing graphene-aluminum nanocomposites. *J. Alloys Compd.* **2018**, *746*, 269–276. [[CrossRef](#)]
20. Li, J.L.; Xiong, Y.C.; Wang, X.D.; Yan, S.J.; Yang, C.; He, W.W.; Chen, J.Z.; Wang, S.Q.; Zhang, X.Y.; Dai, S.L. Microstructure and tensile properties of bulk nanostructured aluminum/graphene composites prepared via cryomilling. *Mater. Sci. Eng. A* **2015**, *626*, 400–405. [[CrossRef](#)]
21. Yolshina, L.A.; Muradymov, R.V.; Korsun, I.V.; Yakovlev, G.A.; Smirnov, S.V. Novel aluminum–graphene and aluminum–graphite metallic composite materials: Synthesis and properties. *J. Alloys Compd.* **2016**, *663*, 449–459. [[CrossRef](#)]
22. Yolshina, V.A.; Yolshina, L.A.; Elterman, V.A.; Vovkotrub, E.G.; Shatunova, A.A.; Pryakhina, V.I.; Khlebnikov, N.A.; Tarakina, N.V. Synthesis of and characterization of freestanding, high-hierarchicallystructured graphene-nanodiamond films. *Mater. Des.* **2017**, *135*, 343–352. [[CrossRef](#)]
23. Yolshina, L.A.; Muradymov, R.V.; Vovkotrub, E.G.; Smirnov, S.V. Diamond synthesis in aluminum matrix in molten alkali-halide at ambient pressure. *Diam. Relat. Mater.* **2015**, *55*, 1–11. [[CrossRef](#)]
24. Yolshina, L.A.; Vichuzhanin, D.I.; Smirnova, E.O. Enhancement of the Mechanical Properties of Aluminum-Graphene Composites. *AIP Conf. Proc.* **2016**, *1785*, 040093.
25. Yolshina, L.A.; Vovkotrub, E.G.; Shatunova, A.A.; Pryakhina, V.I. Raman spectroscopy study of graphene formed by “in situ” chemical interaction of an organic precursor with a Journal Pre-proof molten aluminium matrix. *J. Raman Spectrosc.* **2020**, *51*, 221–231. [[CrossRef](#)]
26. Safina, L.; Baimova, J.; Krylova, K.; Murzaev, R.; Mulyukov, R. Simulation of metal-graphene composites by molecular dynamics: A review. *Lett. Mater.* **2020**, *10*, 351–360. [[CrossRef](#)]

27. Liu, J.; Zhang, Y.Y.; Zhang, H.N.; Yang, J. Mechanical properties of graphene-reinforced aluminium composite with modified substrate surface: A molecular dynamics study. *Nanotechnology* **2021**, *32*, 085712. [[CrossRef](#)] [[PubMed](#)]
28. Zhou, X.; Liu, X.; Lei, J.; Yang, Q. Atomic simulations of the formation of twist grain boundary and mechanical properties of graphene/aluminum nanolaminated composites. *Comp. Mater. Sci.* **2020**, *172*, 109342. [[CrossRef](#)]
29. Sheinerman, A.G. Mechanical properties of metal matrix composites with graphen and carbon nanotubes. *Phys. Met. Metallogr.* **2022**, *123*, 57–84. [[CrossRef](#)]
30. Shirinkina, I.G.; Brodova, I.G.; Rasposienko, D.Y.; Muradymov, R.V.; Yolshina, L.A.; Shorokhov, E.V.; Razorenov, S.V.; Gorkushin, G.V. The effect of graphene additives on the structure and properties of aluminum. *Phys. Met. Metallogr.* **2020**, *121*, 1193–1202. [[CrossRef](#)]
31. Brodova, I.G.; Petrova, A.N.; Shirinkina, I.G.; Rasposienko, D.Y.; Yolshina, L.A.; Muradymov, R.V.; Razorenov, S.V.; Shorokhov, E.V. Mechanical properties of submicrocrystallinealuminium matrix composites reinforced by “in situ” graphene through severe plastic deformation processes. *J. Alloys Compd.* **2021**, *859*, 158387–158395. [[CrossRef](#)]
32. Wu, H.; Huang, M.; Li Xu Xia, Y.; Wang ZhGuohua, F. Temperature-dependent reversed fracture behavior of multilayered TiB_w/Ti–Ti(Al) composites. *Int. J. Plast.* **2021**, *141*, 102998. [[CrossRef](#)]
33. Fu, X.; Tan, Z.; Min, X.; Li, Z.; Yue, Z.; Fan, G.; Xiong, D.-B.; Li, Z. Trimodal grain structure enables high-strength CNT/Al-Cu-Mg composites higher ductility by powder assembly & alloying. *Mater. Res. Lett.* **2020**, *9*, 50–57. [[CrossRef](#)]
34. Vanin, M.; Mortensen, J.J.; Kelkkanen, A.K.; Garcia-Lastra, J.M.; Thygesen, K.S.; Jacobsen, K.W. Graphene on metals: A van der Waals density functions study. *Phys. Rev. B* **2010**, *87*, 081408. [[CrossRef](#)]
35. Sharma, R.; Chadha, N.; Saini, P. Determination of defect density, crystallite size and number of graphene layers in graphene analogues using X-ray diffraction and Raman spectroscopy. *Indian J. Pure Appl. Phys.* **2017**, *55*, 625–629.
36. Shorokhov, E.V.; Zhgilev, I.N.; Valiev, R.Z. Method for Dynamic Deforming of Metals. Abstract of Invention. Patent RU 2283717 C2, 20 September 2006.
37. Brodova, I.G.; Zel'dovich, V.I.; Khomskaya, I.V. Phase-Structural Transformations and Properties of Non-Ferrous Metals and Alloys under Extreme Conditions. *Phys. Met. Metallogr.* **2020**, *121*, 631–663. [[CrossRef](#)]
38. Petrova, A.N.; Brodova, I.G.; Plekhov, O.A.; Naimark, O.B.; Shorokhov, E.V. Mechanical properties and energy dissipation in ultrafine-grained AMTs and V95 aluminum alloys during dynamic compression. *Tech. Phys.* **2014**, *59*, 989–996. [[CrossRef](#)]
39. Razorenov, S.V.; Garkushin, G.N. Hardening of metals and alloys during shock compression. *Tech. Phys.* **2015**, *60*, 1021–1026. [[CrossRef](#)]
40. Brodova, I.G.; Petrova, A.N.; Razorenov, S.V.; Shorokhov, E.V. Resistance of submicrocrystalline aluminum alloys to high-rate deformation and fracture after dynamic channel angular pressing. *Phys. Metals Metallogr.* **2015**, *116*, 519–526. [[CrossRef](#)]
41. Razorenov, S.V. Influence of structural factors on the strength properties of aluminum alloys under shock wave loading. *Matter Radiat. Extrem.* **2018**, *3*, 1–54. [[CrossRef](#)]
42. Barker, L.M.; Hollenbach, R.E. Laser interferometry for measuring high velocities of any reflecting surface. *J. Appl. Phys.* **1972**, *43*, 4669–4675. [[CrossRef](#)]
43. Chen, W.; Yang, T.; Dong, L.; Elmasry, A.; Song, J.; Deng, N.; Elmarakbi, A.; Liu, T.; Bao, L.H.; Qing, F.Y. Advances in graphene reinforced metal matrix nanocomposites: Mechanisms, processing, modelling, properties and applications. *Nanotechnol. Precis. Eng.* **2020**, *3*, 189–210. [[CrossRef](#)]